Towards the optimization of nuclear medicine procedures for better spatial resolution, sensitivity, scan image quality and quantitation measurements by using a new Monte Carlo model featuring PET imaging

George E. Karpetas[1] MSc,
Christos M. Michail[2] PhD,
George P. Fountos[2] PhD,
Pipitsa N. Valsamaki[3] MD, PhD,
Ioannis S. Kandarakis[2] PhD,
George S. Panayiotakis[1] PhD

1. Department of Medical Physics, Faculty of Medicine, University of Patras, 265 00 Patras, Greece
2. Technological Educational Institute (TEI) of Athens Department of Medical Instruments Technology, Ag. Spyridonos, 12210, Athens, Greece
3. Department of Nuclear Medicine, University General Hospital "Alexandra", Athens, Greece

***

Correspondence address:
Assoc. Prof. Dr. G. Fountos
Department of Medical Instruments Technology, Technological Educational Institution of Athens, Ag. Spyridonos Street, Egaleo, 122 10 Athens, Greece.
Tel: (+3010) 5385-375 (work)
E-mail: gfoun@teiath.gr

Abstract

The aim of this study was to develop a Monte-Carlo model that can be used for the optimization of positron emission tomography (PET) procedures and image quality metrics. *This model was developed* using the Monte Carlo package of Geant4 application for tomographic emission (GATE) and the software for tomographic image reconstruction (STIR) with cluster computing to obtain reconstructed images. The PET scanner used in this study was the General Electric Discovery-ST (US). The GATE model was validated by comparing results obtained in accordance with the National Electrical Manufacturers Association NEMA-NU-2-2001 protocol [Mawlawi et al (2004) and Bettinardi et al (2004)]. All images were reconstructed with the commonly used 2D filtered back projection and the 3D reprojection algorithms. *We found* that the simulated spatial resolution in terms of full width at half maximum (FWHM) agreed within less than 3.29% in 2D and less than 2.51% in 3D with published data of others, respectively. The 2D values for the sensitivity, scatter fraction and count-rate were found to agree within less than 0.46%, 4.59% and 7.86%, respectively with these published values. Accordingly, our study showed that the corresponding 3D values were found to agree to less than 1.62%, 2.85% and 9.13%, respectively with Mawlawi et al (2004) published values. Sensitivity, which was also estimated without the presence of attenuation material by simulating an ideal source, showed differences between the extrapolated and the ideal source values (with and without attenuation) ranging in 2D from 0.04% to 0.82% (radial location R=0cm) and 0.52% to 0.67% in 3D mode (radial locations R=10cm). The simulated noise equivalent count rate was found to be 94.31kcps in 2D and 66.9kcps in 3D at 70 and 15kBq/mL respectively, compared to 94.08kcps in 2D and 70.88kcps in 3D at 54.6kBq/mL and 14kBq/mL respectively, from the published by others values. The simulated image quality was found in excellent agreement with these published values. *In conclusion*, our study showed that our Monte Carlo model can be used to assess, optimize, simplify and reduce the simulation time for the quality control procedure of PET scanners. By using this model, sensitivity can be obtained in a more simplified procedure. Reconstructed images by STIR can be also used to obtain radiopharmaceutical distribution of images and direct dose maps, quite useful to nuclear medicine practitioners.

Introduction

Positron emission tomography (PET) scanners have been an essential, functional, imaging modality for various medical disciplines in which the in vivo radiotracer distribution is reconstructed to form a representing image. The PET images are obtained by using the following architecture: Collimators for the scatter reduction usually consisted from retractable tungsten septa (2D mode) between image slices. When these septa are retracted (3D mode) the system allows oblique lines of response to gamma rays. The collimated gamma rays are detected by a scintillating crystal array in the scanning device, creating a burst of light which is detected by photomultiplier tubes (PMT) or silicon avalanche photodiodes (Si APD) [1].

The imaging performance of PET/CT scanners is affected by factors including photon noncollinearity, oblique detector penetration, detector size and response, positron range, photon scatter, and patient motion all of which contribute to the decreased PET system performance [2-4]. These parameters could be accurately modelled by Monte Carlo simulation packages so that in the future high quality scanners for improved images could be developed. Simulations can be used in nuclear medicine imaging for designing imaging protocols and for better interpreting SPET and PET scans [5, 6]. Over the last decade, Monte Carlo methods were extensively used in nuclear medicine, i.e. in PET and in SPET, to model the performance of complete

imaging systems and assist in the design of new emission tomography developments [7, 8]. Simulation codes such as Geant3 (GEometry ANd Tracking) [9], EGS4 (Electron Gamma Shower) [10], MCNP (Monte Carlo N-Particle Transport) [11] and Geant4 [12] were published, modeling high energy physics with well validated physics models, geometry modeling tools, and applying better visualization utilities. Research groups and clinical nuclear medicine users share the need for developing new simulation tools easy to use and with better precision, speed, flexibility and better support of the implemented software [6]. An open-source extension of the Geant4 Monte Carlo toolkit was the GATE (Geant4 Application for Tomographic Emission) package that was developed by the Open-GATE collaboration [13]. Geant4, as the core of the GATE toolkit, is an international open-source project and has the advantage of being able to incorporate new developments in PET and SPET scanners by all users [7, 14].

Several validation studies of GATE models for commercial PET scanners have been reported in the literature [4, 15-17]. The GATE projection data can be converted to three dimensional (3D) sinograms which can then be reconstructed by the software for tomographic image reconstruction (STIR) open source software package in order to obtain 3D PET images [4, 18, 19].

The latest developments in GATE simulations, together with the increased power of computers we now use, make GATE Monte Carlo simulations a popular accessible tool in emission tomography, which can generate realistic complex data for various applications at a reasonable time, contributing in development, validation and support, of the OpenGATE [5, 20]. In this context, GATE model offers the opportunity for more realistic dynamic biodistribution of the tracers, such as respiratory and cardiac motions, displacement of the scanner, such as the rotation of the camera heads in SPET, tracer kinetics, time-of-flight (TOF) PET, radioactive decay, and dead time effects. These features enable us to simulate time curves under realistic acquisition conditions and to test dynamic reconstruction algorithms [20]. GATE also provides the opportunity for PET dosimetry, such as the study of biodistribution of radiotracers using imaging to predict the dose distribution of a therapeutic agent, or modeling the radiotracer heterogeneity in with tumors with PET imaging [20-27]. For instance, dosimetry of Zevalin® (ibritumomab tiuxetan) labeled with yttrium-90, using GATE SPET imaging can be performed as Zevalin® labeled with indium-111 [26]. GATE simulations can be developed further, in order to obtain directly dose maps from the activity biodistribution used as input in Monte Carlo simulations [20].

Furthermore, GATE could be used for the improvement of PET or SPET scanner instrumentation by: a) the simulation of PET cameras using pixellated cadmium zinc telluride, (CdZnTe-CZT) detectors [28], b) the use of dual layer phoswich detectors [29], c) the design of realistic phantoms with compressed voxels for high-resolution phantom simulations [30-32], d) the examination of the impact of the crystal material and size on the PET performance [33] and e) the optimization of image reconstruction, scatter correction and imaging protocols. Furthermore, with GATE are now possible simultaneous simulations of dynamic 4D PET-MR data using anatomic and dynamic information from real MR acquisitions [34].

Various Gate studies have been published on implementing STIR reconstruction simulation for large commercial PET scanners [4, 12, 35-39]. From this point on image quality was assessed by evaluating reconstructed images obtained from the STIR software.

However quality control in PET scanners is in some cases complex and time is an inhibitory factor. For example sensitivity estimation demands a complex and time worthy procedure [40]. Furthermore, the Compton scatter rejection leads to a sensitivity decrease, affecting the acquisition time.

We undertook this study in order to reconstruct medical images of a PET scanner using the GATE Monte Carlo package with the STIR image reconstruction software. Sensitivity, complexity and time issues were addressed by simulating an ideal source, without the presence of attenuation material, as an alternative PET sensitivity measurement, thus simplifying the whole procedure.

The influence of Compton scatter recovery in PET sensitivity was also investigated by increasing the energy window. A more accurate insight in the emission tomography imaging chain was provided, aiming to be easily reproduced in clinical practice and to obtain specific PET images from a known radiopharmaceutical distribution in simplified phantoms or in more complex human structures.

Materials and methods

Geometry of the modeled PET scanner
The scanner modeled in this study was the Discovery ST (US) PET/CT scanner an integrated second generation PET/CT system. The system incorporates bismuth germinate oxide (BGO) crystals of 6.3x6.3x30mm in the axial, transaxial and radial directions, respectively (Fig. 1). The crystals are assembled into 6x6 blocks. Each block is coupled to a photomultiplier tube (PMT) consisting of four square channels, and assembled in modules of 8 blocks (2x4) each. The detector ring is finally comprised of 35 modules, i.e. 280 crystal blocks, or 24 rings of 420 crystals (in a total of 10080 BGO crystals). Ring dimensions are 88.6cm in diameter with a 15.7cm axial and 70cm transaxial field of view (FOV). The scanner was designed to acquire images in both 2D and 3D modes. In 2D mode, collimation between image slices was achieved with retractable tungsten septa (54mm length and 0.8mm thick) which reduce scatter by restricting gamma rays entering the BGO crystals to only those traveling nearly perpendicularly to the axial direction. Thus, every image plane counts events
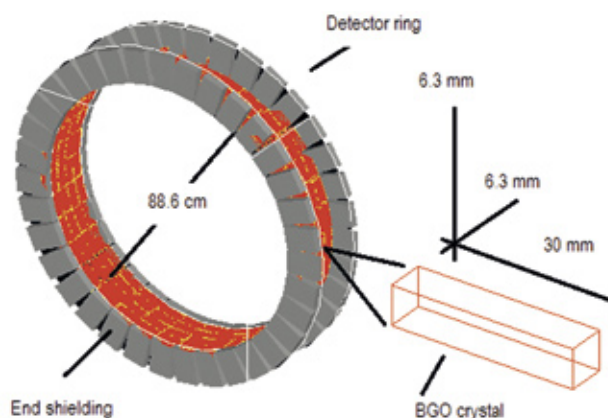

Figure 1. Geometry of the modeled PET scanner.

from ±5 crystal rings in a high sensitivity mode. In 3D mode, the septa were absent and the system allowed oblique lines of response with all the 24 rings. The energy window width in both cases was set from 375 to 650keV with a coincidence timing window of 11.7ns.

Physics processes

The production of secondary electrons (X rays and δrays) in GATE can be settled by thresholds similar with Geant4 [5]. Furthermore GATE uses the standard and low-energy Geant-4 packages in order to simulate electromagnetic processes [5]. In this study, the standard energy package was used to model the photoelectric and Compton interactions and the low-energy package to simulate the Rayleigh interactions. The following energy and range cuts, for photons and electrons, were used [7]: electron range =30cm, δray =1GeV and Xray =1GeV.

Signal processing (or Digitizer chain)

GATE simulation is extended beyond physics processes, upon the scanner's detectors and the signal processing chain. In order to accomplish this, a series of signal processors were used referring as *the Gate Digitizer* object or Digitizer. The Digitizer was composed of different modules that may be inserted into the linear signal processing chain to process photon interactions that produce single events from which the coincidence events are formed. Every Digitizer's signal processed mimics a separate segment of the simulated PET scanner's signal processing chain [4]. Then the particles interact within an individual crystal and an *Adder* module sums the deposited energy to yield a pulse. Following this, a *Readout* module regroups pulses for every block of crystals in order to create a final pulse per photon detected. Afterwards, a Gaussian energy blur, with an average energy resolution for each crystal of the detector block of 17% referenced at 511keV, is attributed by a *Crystal Blurring* module applying a Quantum Detection Efficiency (QDE) of 0.94 at 511keV [41, 42]. Next, a 300ns dead time value is applied on the single events in the BGO crystal [43, 44] by a paralysable *Deadtime* module. Then, at the same level, an *Energy Window* discriminator between 375 and 650keV is applied via the *Tresholder* and *Upholder* modules, both incorporated within the energy window. The chain describing single events as above can result in the creation of nine types of files, in order to be used for various applications which require the specific file types. These file types contain the detected single events and can be enabled or disabled, when needed. For each single event they contain data about the energy deposited in the crystal and the coordinates of detection within the modeled scanner geometry. These file types are: 1) the American Standard Code for Information Interchange (*ASCII*), 2) the *root* file containing four histograms and four tree files (gate, coincidence, hits and singles), 3) the *online plotter* which allows online display of several variables, 4) the *interfile* projection set designed to mimic an acquisition protocol for multiple headed gamma cameras, 5) the *sinogram* output file which is the 2D array of data containing projections, 6) the *ECAT7* binary format which uses data blocks for the header information, 7) the List Mode Format (*LMF*), 8) the *imageCT* output which is a binary matrix of float numbers that stores the simulated CT image, and 9) the *raw* output file which is stored in binary format and provides access to raw images [45].

In this study the root output file [46] was selected, in order to obtain the validation results in the sense of spatial resolution, sensitivity and noise equivalent count rate (NECR) according to the NEMA protocol [35]. The sinogram output file (.ima), obtained from the ECAT system, is a raw data file (unsigned short integer), used by STIR as input file for the reconstruction of the simulated flood source image [45]. All evaluations of this study were performed on the central slice of the reconstructed images. Once these files were created, a second processing stage was inserted, aiming to search the *Singles'* list for coincidences within a given time, which is called "the coincidence time window". The module which is responsible for the aforementioned process is the *Coincidence Sorter* defined in the digitizer chain terminology, leading to the creation of a *Coincidence file*. In this study on the GE DST PET/CT scanner, the coincidence time window was set to 11.7ns. All simulations were obtained using a computer cluster with 12 dual core Intel(R) Xeon(TM) CPU 3.00GHz processors (Supermicro SuperServer 6015B-UR/NTR, UK).

Coincidence processing

The event identification (ID) number, which uniquely identifies the annihilation event from where each single is coming and the number of Compton interactions that have occurred during the tracking of each photon are also stored in the Singles list [45]. The event ID number and the number of the Compton interactions were used in the classification of random, trues and scattered coincidences [45].

Evaluation protocols NEMA NU 2-2001 (N-01) measurements

All simulations performed in this work, were obtained following the NEMA 2001 protocol under both 2D and 3D modes [35] as stated below.

Spatial resolution

Spatial resolution of the GE Discovery ST (DST) was simulated by using six point sources of ^{18}F- FDG with concentration >80MBq/mL, positioned at six points. These six points were two groups of three, one group at the center of the field of view and the second group shifted by one fourth of the FOV, at positions: x=0cm, y=1cm; x=0cm, y=10cm; and x=10cm, y=0cm in the FOV of the scanner, according to NEMA NU 2-2001 protocol [35, 47]. The positron sources were inside glass capillaries with ID of 1mm. Both 2D and 3D mode data were acquired. Following the above, in both 2D and 3D modes, the images were reconstructed using STIR with the 3D filtered back projection (FBP3DRP) algorithm
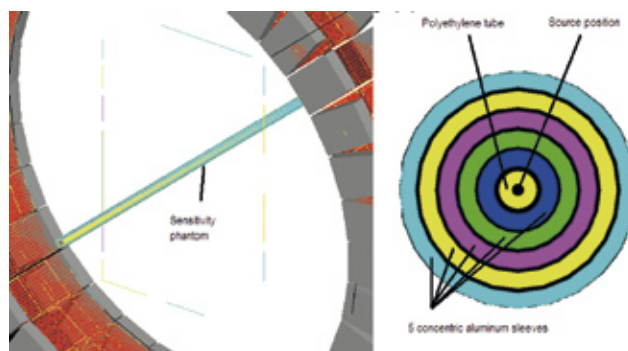

Figure 2. Sensitivity phantom.

using Colsher filter with additional apodizing window 0.5 [48, 49]. Spatial resolution was determined by measuring both the full width at half maximum (FWHM) and the full width at tenth maximum (FWTM) of the point spread functions PSFs in all three orthogonal directions, according to the NEMA 2001 protocol [35].

Sensitivity
The sensitivity of a scanner represents its ability to detect annihilation of radiation. In the NU 2-2001 standard, the absolute sensitivity of a scanner is expressed as the rate of detected coincidence events in counts per second (cps) for a given source activity, in MBq. Since the emitted positrons annihilate with electrons to create pair(s) of γ-rays, a significant amount of material (for example aluminum) must surround the source to ensure annihilation. The positron annihilation distance for ^{18}F is less than 0.5mm while few positrons annihilate at distances of more than 1mm. The surrounding material also attenuates the created γ-rays, prohibiting a simulation without interfering attenuation. To achieve an attenuation-free value of the sensitivity, successive simulations were made with a uniform line source surrounded by known absorbers. The sensitivity without absorbers can be obtained by linear extrapolation to the successive sensitivity values, obtained from each absorber in Figures 5 and 6 [2]. The sensitivity of the scanner was modeled by simulating a 70cm long plastic tube with 5 aluminum sleeves, filled with a known amount of radioactivity and defined in the center of the transverse FOV. A ^{18}F source was used with activity of 9.25MBq (Fig. 2) [2]. This radioactivity is sufficiently low so that count losses due to deadtime and randoms coincidences are negligible. The central polyethylene tube has an internal diameter of 1mm and an external diameter of 3mm [2]. Data were acquired in 2D and 3D modes. Afterwards, the source and sleeves were placed at 10cm off the central axis and acquisition was repeated.

Sensitivity was also obtained with a broadened energy window 200-650keV in order to investigate the impact of Compton scatter recovery [50]. For comparison purposes an ideal source with no attenuation was also modeled with source activity of 9.25MBq and external diameter of 3mm, in order to validate the accuracy of the NEMA sensitivity extrapolation method.

Scatter fraction and count rates
A cylindrical polyethylene phantom of 70cm length and 20cm diameter with an internal 3.1cm circular opening, parallel to its central axis was modeled (Fig. 3) [35]. The hole
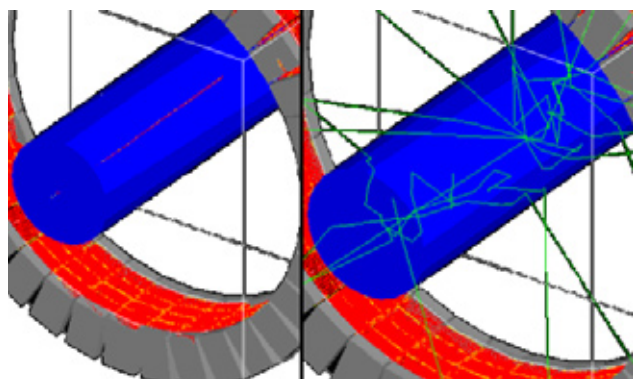
was located at a radius of 4.5cm off the central axis of the phantom. A Teflon line source with solution of water and ^{18}F with activity of 100kBq/mL and 35kBq/mL for the 2D and 3D respectively, with internal diameter of 2.3mm was defined in the hole.

The simulation was performed for both 2D and 3D modes. The phantom was simulated at the center of the FOV. Data acquisition was recorded without delayed-event randoms data. The simulated phantom was scanned over a period of 12h and imaged repeatedly in 2D and 3D modes for each activity point. A total of 24 2D and 24 3D data acquisition frames were recorded and each frame was recorded for 15min with no delay between consecutive acquisitions. The raw data with no corrections applied were then reconstructed into sinograms. The average system scatter fraction, as well as the scatter fraction for each slice across the axial FOV were then calculated and plotted according to the NU 2-2001 protocol [35]:

$$SF = S / (S + T) \quad (1)$$

where S and T are the number of true and scattered coincidences.

The counting rate performance of the scanner was evaluated using all data acquisition time points. The total system counting rate (trues, random, and scatter event rates) as well as the noise equivalent counting rates (NECR) were then calculated:

$$NECR = T^2 / (T + S + kR) \quad (2)$$

where R is the number of random coincidences. A k value of 1 during the direct measurements of NECR rates was used denoting a noiseless random correction [35]. Peak values and corresponding activity concentration, for these rates, were also determined according to the NEMA NU 2-2001 protocol [35].

Image quality
Image quality, in both 2D and 3D modes, was evaluated by simulating the NEMA/IEC torso phantom. The phantom contains six co-axial isocentric spheres (Fig. 4) [35]. A cylindrical insert of 5cm diameter was positioned in the cen-
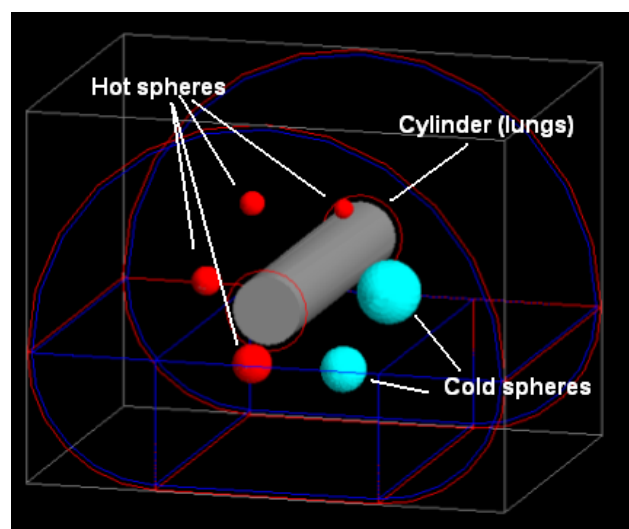

Figure 3. Left: NEMA phantom. Right: acquisition starts.

Figure 4. NEMA/IEC torso phantom.

tre of the phantom (Fig. 4). The cylinder was simulated as a cold insert with a density of 0.30g/mL, to simulate the lungs. Four of the spheres with diameters 1.0, 1.3, 1.7 and 2.2cm were used to simulate hot lesions, while the other two (2.8 and 3.7cm) were used to simulate cold lesions. The background of the phantom was filled with 6kBq/mL of ^{18}F-FDG whereas the hot spheres were filled with an activity four times greater than the background activity (i.e. 24kBq/mL).

The obtained images were acquired using STIR, after reconstruction of the arc corrected sinogram data with the Kinahan and Rogers (1989) FPB3DRP (3D Reprojection) [48, 49, 51] using by default a Colsher filter with additional apodizing window with a cutoff frequency at 0.5 cycles [48]. FPB3DRP reprojection method was used to account for the problem of axial shift variance or truncation of the projection data. A first estimate of the image was reconstructed using a sufficient data set with all projections (usually the set of transaxial or direct projections) fully measured. By calculating line integrals through this first image, along the missing detection channels, the truncated parts of the projections can be recovered at all remaining angles. This was obtained by forward-projecting from a first image estimate what would have been detected by an axially longer scanner. Having artificially restored the axial shift invariance of the data, the image was then reconstructed by filtered backprojection (FBP) of the 2D projections using the Colsher filter [49]. The amide's medical imaging data examiner (AMIDE) viewer was used to read the STIR image data [48].

Attenuation correction was performed according to the method described by Zaidi and Hasegawa (2003) [52] with perfect scatter rejection. Attenuation correction was performed by applying the attenuation correction factors (ACF) of the created attenuation map on the reconstructed image [52].

The sinograms of the projections were defined by 47 segments, bin size 0.3195cm, 221 arc-corrected and 249 non arc-corrected bins, span 3 and mashing 1. The hot and cold sphere contrast for each sphere size was then calculated according to the NEMA NU 2-2001 protocol. From these images the hot and cold sphere percentage contrast was calculated as:

$$Q_{h,j} = \frac{(C_{h,j} / C_{b,j}) - 1}{(A_h / A_b) - 1} \cdot 100\% \qquad (3)$$

and

$$Q_{c,j} = (C_{c,j} / C_{b,j} - 1) \cdot 100\% \qquad (4)$$

where $Q_{h,j}$ and $Q_{c,j}$ are the hot and cold sphere percentage contrast, $C_{h,j}$ and $C_{c,j}$ are the count densities of the hot and cold spheres, $C_{b,j}$ is the count density of the background for sphere j, A_h is the activity concentration in the hot sphere and A_b is the background concentration activity [35].

The percent bg variability N for sphere j is calculated as:

$$N_j = SD_j / C_{b,j} \cdot 100 \qquad (5)$$

where SD_j is the standard deviation of the background for sphere j, calculated as:

$$SD_j = \sqrt{\sum_{k=1}^{K} (C_{b,j,k} - C_{b,j})^2 / (K-1)}, K = 60 \qquad (6)$$

Finally, in the image quality estimation, the residual error due to scatter and attenuation corrections ($\Delta C_{lung,i}$) in percentage units for each slice i, shall be calculated as follows:

$$\Delta C_{lung,i} = C_{lung,i} / C_{b,i} \cdot 100\% \qquad (7)$$

where $C_{lung,i}$ is the count density in the lung insert.

Results

Spatial resolution

Table 1 shows a comparison between the spatial resolution obtained from the GATE simulations and the published experimental data [2, 47]. Spatial resolution was assessed in both axial and transverse directions, according to NEMA NU 2-2001 protocol [35]. The differences between simulated results and experimental FWHM data [2, 47] range from 0.16%-3.28% in 2D and from 0.33%-3.29% in 3D modes. The corresponding differences of the FWTM data range from 0.17%-0.86% in 2D and 0.17%-1% in 3D modes. In all cases, 2D FWHM and FWTM were lower than the corresponding 3D values, due to the collimators used in the 2D set-up that determines a narrower FOV, which in turn provides better resolution properties.

Sensitivity

Figures 5 and 6 show a comparison of the simulated system's count rate with experimental data [2] in both 2D and 3D, at radial locations R=0 and R=10cm. The attenuation coefficient of the aluminum sleeve was found equal to 0.1097/cm in 2D mode and 0.073/cm in 3D mode, by using the exponential law, after extrapolation of the system events counting rate (Fig. 5, 6) [35]. The extrapolated values, obtained after linear regression to the data of Figs. 5 and 6, were used to calculate the total counting rate in the absence of any attenuating material (no wall thickness). The difference in linear attenuation coefficient of the Al sleeve between 2D and 3D (0.1097 for 2D and 0.073 cm^{-1} for 3D), calculated according to the sensitivity measurement of the NEMA protocol, was attributed to the septa, present in 2D [53]. Accurate determination of the linear attenuation coefficient requires narrow beam geometry conditions [52]. These conditions are more similar with the 2D geometry rather than the 3D, in which geometry is closer to conditions measuring energy absorption coefficient (0.077cm^{-1} at 511keV for Al) [54]. The linear attenuation coefficient of aluminum (0.22/cm) was calculated from tabulated data on attenuation coefficients (0.08cm^2/g at 511keV) and density (2.7g/cm^3), which have been obtained with narrow beam geometry [54]. The ratio of the total counting rate to the administered activity equals the system's sensitivity, which is shown in Table 2. This table shows a comparison of the simulated system's sensitivity with experimental data [2] in both 2D and 3D, at radial locations R=0 and R=10cm. The differences between simulated and experimental [2] sensitivity values are shown in Table 2 ranging from 0.06% to

Table 1. *Simulated and measured spatial resolution*

		Spatial resolution							
		y-coordinate (cm)							
		1	10	1	10	1	10	1	10
		FWHM (mm)				FWTM (mm)			
2D	Axial	5.01[a]	6.10[a]	5.18[b]	6.12[b]	9.28[a]	12.31[a]	9.33[c]	12.35[c]
	Transverse Radial	6.22[a]	6.75[a]	6.13[b]	6.72[b]	11.45[a]	12.33[a]	11.55[c,d]	12.38[c]
	Transverse Tangential	6.12[a]	6.88[a]	6.13[b]	6.99[b]	11.53[a]	13.09[a]		13.12[c]
3D	Axial	5.82[a]	6.47[a]	5.97[b]	6.69[b]	11.87[a]	11.48[a]	11.94[c]	11.52[c]
	Transverse Radial	6.25[a]	6.81[a]	6.11[b]	6.77[b]	11.47[a]	12.59[a]	11.49[c,d]	12.68[c]
	Transverse Tangential	6.13[a]	6.89[a]	6.11[b]	6.78[b]	11.44[a]	11.82[a]		11.94[c]

a. This work, b. Reference 1, c. Reference 28, d. Radial and Tangential average.

Table 2. *System sensitivity in 2D and 3D modes*

	Sensitivity (cps/kBq)					
	Simulated (GATE)		Experimental[a]		Deviations (%)	
Radial location (cm)	2D	3D	2D	3D	2D	3D
0	1.94	9.03	1.93	9.17	0.46	1.62
10	1.99	9.28	1.98	9.42	0.06	1.51

a: Reference [2].

1.62% in both 2D and 3D modes. The differences between the extrapolated and the ideal source values (with and without attenuation) range from 0.04% to 0.82% (radial location R=0cm) in 2D and 0.52% to 0.67% (radial locations R=10cm) in 3D mode. Taking this into account, the sensitivity simulations could be obtained only from the ideal source simplifying the NEMA sensitivity method and reducing the simulation time.

Figures 7 and 8 show the 2D and 3D sensitivity profiles across the axial FOV of the scanner, in the centre (0cm) and for radial position 10cm off the central axis. Summation of the true events contained in the 47 planes provides also verification of the system sensitivity, as shown in Table 2. By increasing the energy window and thus allowing more scattered events to contribute as useful signal (besides the 40% of the interactions that fall within the photo peak at 511keV in the 375-650keV energy range) [43], sensitivity was further improved by the following ratios: (i) 1.34 at radial location of 0cm, and 1.31 at 10cm, in 2D mode (25.37% increase at 0cm and 23.82% at 10cm), (ii) 1.17 at 0cm, and 1.17 at 10cm, in 3D mode (14.58% increase at 0cm and 14.81% at 10cm).

Counting rate performance

Figures 9 and 10 show the counting rate performance of the scanner in 2D and 3D, modes compared to published data [2] for activity concentration of 100 and 35kBq/mL for the 2D and the 3D, respectively. The simulated 2D true coincidences were higher than 307.17kcps, whereas the 2D randoms were higher than 1100.23kcps, at 100kBq/mL, respectively. The 2D peak scatter count rates, in 2D, were 82.83kcps at 100kBq/mL. The corresponding simulated 2D peak NECR was 94.31kcps at 70kBq/mL. For the 3D data acquisition mode, the simulated true, random and scatter count rates were greater than 352.21, 1800.34 and 273.07kcps at 35kBq/mL, respectively. The corresponding simulated 3D peak NECR was 66.93kcps at 15kBq/mL. Deviations between simulated model count rate values and measured data [2] for activity concentration up to 100kBq/mL (35kBq/mL) in 2D (3D) were smaller than 7.76% (9.13%).
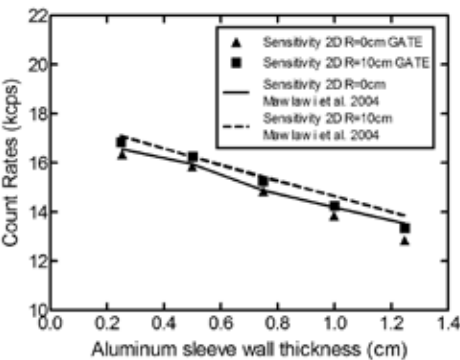

Figure 5. 2D System count rate with the phantom positioned at R=0cm and at R=10cm with respect to the centre of the scanner FOV.
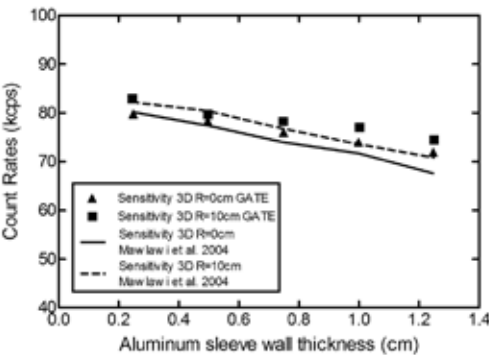

Figure 6. 3D System count rate with the phantom positioned at R=0cm and at R=10cm with respect to the centre of the scanner FOV.

Table 3. *Image quality in 2D and 3D according to NEMA NU 2-2001*

	Image quality											
	Sphere diameter (mm)	1		1.3		1.7		2.2		2.8		3.7	
2D	Hot sphere contrast (%)	29[a]	27[b]	47[a]	53[b]	64[a]	63[b]	75[a]	82[b]	-	-	-	-
	Cold sphere contrast (%)	-	-	-	-	-	-	-	-	66[a]	66[b]	71[a]	73[b]
	Background variability (%)	7[a]	7[b]	7[a]	6[b]	6[a]	6[b]	5[a]	5[b]	3[a]	4[b]	3[a]	3[b]
	Average residual error over 'lung' insert (%)	20%											
3D	Hot sphere contrast (%)	24[a]	22[b]	40[a]	40[b]	52[a]	55[b]	67[a]	71[b]	-	-	-	-
	Cold sphere contrast (%)	-	-	-	-	-	-	-	-	66[a]	65[b]	68[a]	67[b]
	Background variability (%)	5[a]	5[b]	4[a]	5[b]	3[a]	4[b]	3[a]	3[b]	2[a]	2[b]	2[a]	2[b]
	Average residual (%) over 'lung' insert	15%											

a. This work, b. Reference [2].
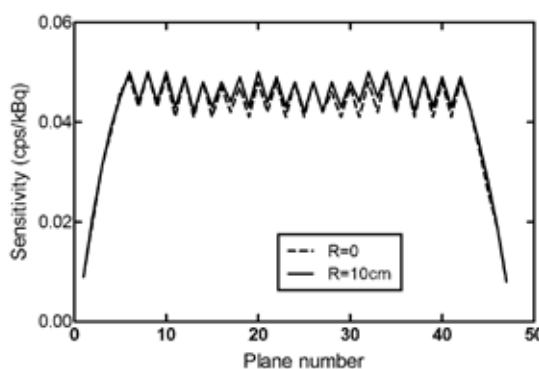
Figure 7. Sensitivity across axial FOV of scanner simulated according to NEMA NU01 standard in 2D data acquisition mode.
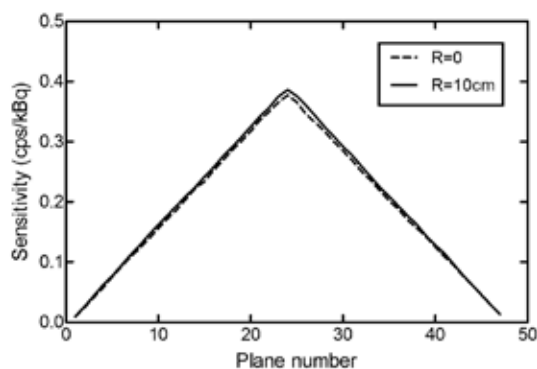
Figure 8. Sensitivity across axial FOV of scanner simulated according to NEMA NU01 standard in 3D data acquisition mode.
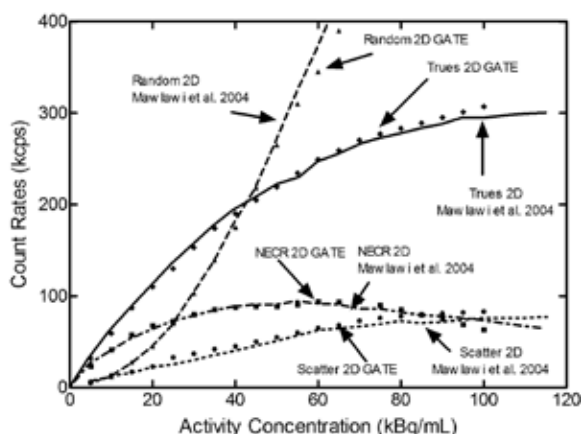
Figure 9. Simulated and measured 2D count rate performance (true, scatter and random coincidences, as well as the NECR).
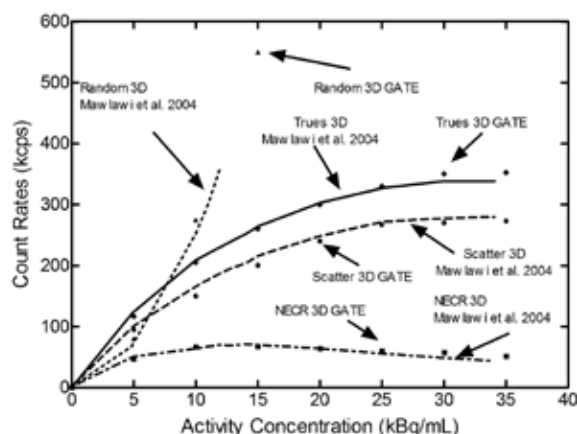
Figure 10. Simulated and measured 3D count rate performance (true, scatter and random coincidences, as well as the NECR).

Scatter fraction

The average scatter fraction estimated by the ratio of the scattered events to the sum of the scattered and true events in 2D and 3D was 20.02% and 43.85%, whereas the measured data were 19.1% and 45.1%, respectively [2].

Image quality

The image quality results in both 2D and 3D, obtained from the simulated torso image quality phantom are shown in Fig. 11 and summarized in Table 3. Hot and cold sphere contrast, as well as the background variability in the lung, are higher

in 2D than in 3D. The average residual error over the 'lung' insert was found 20% in 2D and 15% in 3D.
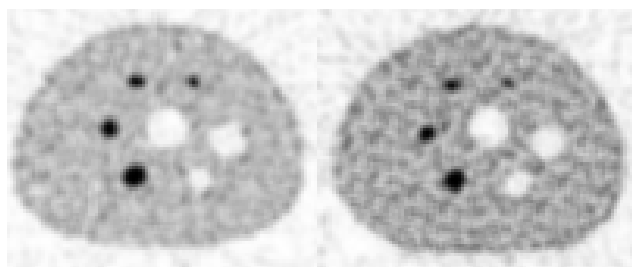

Figure 11. Image quality torso phantom in 2D (left) and 3D (right).

An application of this GATE model on complex human structures is shown in Fig. 12, where the grey scales have been translated to activity distributions. In order to obtain these slices, a brain phantom (Hoffman) [55, 56] was used for simulation. The brain slices were acquired from STIR, after reconstruction of the arc-corrected sinogram data with the commonly used 2D filtered back projection (FBP2D) (Ramp filter with additional apodizing window 0.5) [18, 46] the Kinahan and Rogers FPB3DRP (Colsher filter with additional apodizing window 0.5) and with the iterative, Maximum Likelihood Estimation Ordered Subsets version of Green's MAP One Step Late (MLE-OSMAPOSL) reprojection algorithms [48, 49, 51].
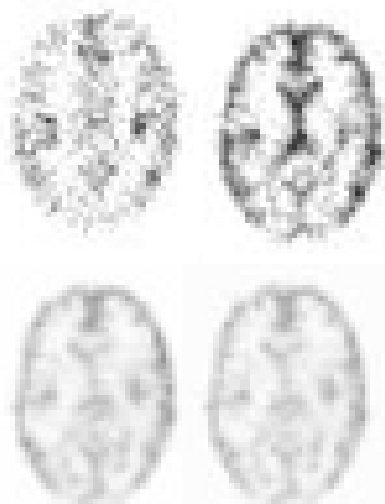

Figure 12. Hoffman brain phantom in 2D (upper left), 3D (upper right), OSEM with 15 subsets/3 iterations (down left) and 21 subsets/3 iterations (down right).

Interpretation of results

In this study, sensitivity was estimated without the presence of attenuation material by simulating an ideal source in order to validate the accuracy of the NEMA sensitivity extrapolation method. The ideal source simulation results showed excellent agreement with those obtained from the extrapolation method. Taking this agreement into account we suggested that simulations for sensitivity could be obtained just from an ideal source simplifying the method and reducing simulation time.

The influence of Compton scatter recovery was also investigated showing that sensitivity can be further improved from 14.58% to 25.37% by increasing the energy window.

Image quality was also assessed by simulations of the IQ torso phantom using the STIR reconstruction software. The simulated image quality was also found in excellent agreement with Mawlawi et al (2004) published data [2].

Furthermore, the STIR reconstructed GATE simulated data were used to obtain PET images from specific radiopharmaceutical distribution using simplified phantoms or more complex human structures. The above results will assist nuclear medicine physicians, as an efficient diagnostic tool.

On a pre-clinical level any potential imaging agent can first be controlled in a fast and straightforward manner. In addition, relevant clinical applications would include: a) novel and worth mentioning imaging protocols for simpler and faster quantitative interpretation of SPET and PET scans, with better anatomical correlation. b) The STIR reconstructed images, could also be used to bridge the gap between imaging and dosimetry, in order to obtain directly dose maps from the activity distribution as input for PET and SPET Monte Carlo simulations. From the latter, physicians could directly compare the actual dose biodistribution map of a tracer, used for the production of SPET or PET data, with the data estimated from the reconstructed PET or SPET images.

Dosimetry on pre-treatment scans in terms of target and dose-limiting tissue uptake determination for optimal targeted radionuclide treatment conditions and for dose reduction to essential levels, could also be assessed [57]. Considering that the increasing nuclear medicine therapeutic applications, have known drawbacks regarding dosimetric issues even in case of γ-emitting radionuclides, the clinical benefit by the use of the model we suggest in this study would be quite important for example, the simplified exact determination of tumour-absorbed dose and toxicity limits, when administering peptide receptor radionuclide treatment (PRRT) with ^{90}Y- or lutetium (^{177}Lu)-labeled somatostatin analogues, or ^{131}I-MIBG treatment in patients bearing neuroendocrine tumours [58-62].

At last, on conventional SPET images, image interpretation is mostly qualitative, except for certain examinations, like Datscan, for which regions of interest (ROI) with corresponding count rates are utilized to produce formula-based values for comparison with reference values. In ^{18}F-FDG-PET, a powerful oncology tool, images are also generally interpreted qualitatively. Both the PET associated semi-quantitative parameter of standardized uptake value (SUV) and the SPET computed values vary with the use of an average pixel value versus a maximum pixel value for each ROI, besides several other parameters. Uniformity of SPET computed values and SUV by using the model dose maps would allow for a quantitative SPET and ^{18}F-FDG-PET image evaluation and subsequent feasibility for direct interstudy comparison [63-65]. Overall this model would allow for faster and more precise detection, e.g. of parathyroid adenomas using ^{99m}Tc-sestamibi (double phase or subtraction) scintigraphy, as well as for avoiding potential pitfalls such as focal uptake in brown fat with ^{18}F-FDG-PET and focal uptake in the bowel due to physiological excretion in ^{67}Ga-citrate or ^{111}In-DTPA-octreotide used for scintigraphies [63-65].

In conclusion, in this study radionuclide medical images of a commercial PET scanner determined by a simulation method of a Monte Carlo model were validated. Our study showed that: a) the simulated spatial resolution (FWHM), sensitivity, scatter fraction, count-rate and simulated noise equivalent count rate (NECR) in 2D and 3D were in close agreement, with others' published experimental values, b)

the STIR reconstructed GATE simulated data as the ones we have used in the present study can be used to obtain realistic PET images, that can be used as a more accurate and simplified diagnostic tool for the improvement of image quality, c) physicians could directly compare the actual dose biodistribution map of a tracer of PET or SPET images, reducing the cost and time for consuming new radiopharmaceuticals, as well as improving the possibility for quantitative measurements of SPET and PET studies.

Bibliography

1. Humm J, Rosenfeld A, Del Guerra A. From PET detectors to PET scanners. *Eur J Nucl Med Mol Imaging* 2003; 30: 1574-97.

2. Mawlawi O, Podoloff D, Kohlmyer S et al. Performance Characteristics of a Newly Developed PET/CT Scanner Using NEMA Standards in 2D and 3D Modes. *J Nucl Med* 2004; 45: 1734-42.

3. Bushberg J, Siebert J, Leidholdt E et al. *The essential physics of medical imaging*. (Lippincott Williams & Wilkins, Philadelphia 2002), 577-749.

4. Schmidtlein C, Kirov A, Nehmeh S et al. Validation of GATE Monte Carlo simulations of the GE Advance/Discovery LS PET scanners. *Med Phys* 2006; 33(1): 198-208.

5. Santin G, Strul D, Lazaro D et al. GATE: A Geant4-based simulation platform for PET, SPECT integrating movement and time management. *IEEE Trans Nucl Sci* 2003; 50: 1516-21.

6. Santin G, Staelens S, Taschereau R et al. Evolution of the GATE project: new results and developments. *Nucl Physics B* 2007; 172: 101-3.

7. Jan S, Santin G, Strul D et al. GATE: A simulation toolkit for PET and SPECT. *Phys Med Biol* 2004; 49: 4543-61.

8. Kalantari F, Rajabi H, Saghari M. Quantification and reduction of attenuation related artifacts in SPET by applying attenuation model during iterative image reconstruction: A Monte Carlo study. *Hell J Nucl Med* 2011; 14(3): 278-83.

9. Brun R, Bruyant F, Maire M et al. *GEANT3* Technical Report. European Organization for Nuclear Research (CERN) DD/EE/84-1, 1987, pp.1-467.

10. Electron Gamma Shower *(EGS)* transport code: http://irs.inms.nrc.ca/software/egsnrc/ 1983.

11. Monte Carlo N-Particle *(MCNP)* transport code: http://mcnp.lanl.gov/ 1987.

12. Geometry And Tracking *(Geant)* transport code: http://www.cern.ch/geant4 1999.

13. Strul D, Santin G, Lazaro D et al. GATE (Geant4 application for tomographic emission): A PET/SPECT general purpose simulation platform. *Nucl Phys* 2003; B 125: 75-9.

14. Agostinelli S, Allison J, Amako K et al. Geant4-A simulation toolkit. *Nucl Instrum Methods Phys Res A* 2003; 506: 250-303.

15. Guerin B, Fakhri G. Realistic PET Monte Carlo Simulation With Pixelated Block Detectors, Light Sharing, Random Coincidences and Dead-Time Modeling. *IEEE Trans Nucl Sci* 2008; 55(3): 942-51.

16. Lamare F, Turzo A, Bizais Y et al. Validation of a Monte Carlo simulation of the Philips Allegro/GEMINI PET systems using GATE. *Phys Med Biol* 2006; 51: 943-62.

17. Gonias P, Bertsekas N, Karakatsanis N et al. Validation of a GATE model for the simulation of the Siemens biograph™ 6 PET scanner. *Nucl Instrum Methods Phys Res A* 2007; 571: 263-6.

18. Thielemans K, Mustafovic S, Tsoumpas C. *STIR: Software for tomographic image reconstruction release 2.* Nuclear Science Symposium Conference Record, IEEE, San Diego, 2006; 4: 2174-6.

19. Nehmeh S, Zeftawy H, Greco C et al. An iterative technique to segment PET lesions using a Monte Carlo based mathematical model. *Med Phys* 2009; 36(10): 4803-9.

20. Buvat I, Lazaro D. Monte Carlo simulations in emission tomography and GATE: an overview. *Nucl Instr Meth Phys Res A* 2004; 569: 323-9.

21. Stute S, Vauclin S, Necib H et al. Realistic and efficient modeling of radiotracer heterogeneity in Monte Carlo simulations of PET images with tumors. *IEEE Trans Nucl Med* 2012; 59: 113-22.

22. Maigne L, Perrot Y, Schaart DR et al. Comparison of GATE/GEANT4 with EGSnrc and MCNP for electron dose calculations at energies between 15keV and 20MeV. *Phys Med Biol* 2011; 56: 811-27.

23. Thiam CO, Breton V, Donnarieix D et al. Validation of a dose deposited by low energy photons using GATE/GEANT4. *Phys Med Biol* 2008; 53: 3039-55.

24. Ferrer L, Chouin B, Bitar A et al. Implementing dosimetry in GATE: dose point kernel validation with GEANT4 4.8.1. *Cancer Biother Radiopharm* 2007; 22: 125-9.

25. Taschereau R, Chatziioannou AF. Monte Carlo simulations of absorbed dose in a mouse phantom from 18-fluorine compounds. *Med Phys* 2007; 34: 1026-36.

26. Visvikis D, Bardies M, Chiavassa S et al. Use of the GATE Monte Carlo package for dosimetry applications. *Nucl Instrum Meth A* 2006; 569: 335-40.

27. Ljungberg M, Frey E, Sjogreen K et al. 3D absorbed dose calculations based on SPECT: evaluation for ^{111}In/^{90}Y therapy using Monte Carlo simulations. *Strand Cancer Biother Radiopharm* 2003; 18: 99-107.

28. Visvikis D, Lefevre T, Lamare F et al. Monte Carlo based performance assessment of different animal PET architectures using pixellated CZT detectors. *Nucl Instrum Meth A* 2006; 569: 225-9.

29. Chung YH, Choi Y, Cho GS et al. Optimization of dual layer phoswich detector consisting of LSO and LuYAP for small animal PET. *IEEE Trans Nucl Sci* 2005; 52: 217-21.

30. Taschereau R, Chatziioannou AF. Compressed voxels for high-resolution phantom simulations in GATE. *Mol Imaging Biol* 2008; 10: 40-7.

31. Zubal IG, Harrell CD, Smith E et al. Computerized three-dimensional segmented human anatomy. *Med Phys* 2004; 21: 299-302.

32. Pretorius PH, Xia W, King MA et al. Evaluation of right and left ventricular volume and ejection fraction using a mathematical cardiac torso phantom. *J Nucl Med* 1997; 38: 1528-35.

33. Ghazanfari N, Sarkar S, Loudos G, Ay MR. Quantitative assessment of crystal material and size on the performance of rotating dual head small animal PET scanners using Monte Carlo modeling. *Hell J Nucl Med* 2012; 15: 33-9.

34. Tsoumpas C, Buerger C, King AP et al. Fast generation of 4D PET-MR data from real dynamic MR acquisitions. *Phys Med Biol* 2011; 56: 6597-613.

35. NEMA standards publication NU 2-2001: *Performance measurements of positron emission tomographs*. Technical report National Electrical Manufactures Association, Washington, DC, 2001.

36. Thielemans K, Tsoumpas C, Mustafovic S et al. STIR: software for tomographic image reconstruction release 2. *Phys Med Biol* 2012; 57: 867-83.

37. Polycarpou I, Marsden P, Tsoumpas C, Evaluation of two approaches to motion-corrected PET image reconstruction. *J of Physics* 2011; 317: 012001.

38. Weber S, Morel C, Simon L et al. Image reconstruction for the ClearPETTM Neuro. *Nucl Instrum Methods Phys Res A* 2006; 569: 381-5.

39. Delso G, Martinez M, Torres I et al. Monte Carlo simulations of the count rate performance of a clinical whole-body MR/PET scanner. *Med Phys* 2009; 36(9): 4126-35.

40. Karakatsanis N, Sakellios N, Tsantilas N et al. Comparative evaluation of two commercial PET scanners, ECAT EXACT HR+ and Biograph 2, using GATE. *Nucl Instrum Methods Phys Res A* 2006; 569: 368-72.

41. Boone J. In: *Handbook of Medical Imaging: Physics and Psychophysics,* edited by J. Beutel, H. L. Kundel, R. L. Van Metter (SPIE, Bellingham, WA, 2000), Vol. 1, pp 36-57.

42. Michail C, Fountos G, Liaparinos P et al. Light emission efficiency and imaging performance of Gd_2O_2S: Eu powder scintillator under X-ray Radiography conditions. *Med Phys* 2010; 37(7): 3694-703.

43. Van Eijk CWE. Inorganic scintillators in medical imaging. *Phys Med Biol* 2002; 47: R85-R106.

44. Valais I, Michail C, David S et al. Luminescence emission properties of $(Lu,Y)_2SiO_5$:Ce (LYSO:Ce) and $(Lu,Y)AlO_3$:Ce (LuYAP: Ce) single crystal scintillators under x-ray medical image conditions. *IEEE Trans Nucl Sci* 2008; 55(2): 785-9.

45. *OpenGATE Collaboration*: http://www-lphe.epfl.ch/GATE.

46. Brun R, Rademakers F. ROOT - An object oriented data analysis framework. *Nucl Instrum Methods Phys Res A* 1997; A 389: 81-6.

47. Bettinardi V, Danna M, Savi A et al. Performance evaluation of the new whole-body PET/CT scanner: Discovery ST. *Eur J Nucl Med Mol Imaging* 2004; 31: 867-81.

48. Thielemans K, Sauge D, Labbe C et al. STIR Software for Tomographic Image Reconstruction User's Guide Version 2.2: http://stir.sourceforge.net/documentation/STIR-UsersGuide.pdf (2012) pp.1-69.

49. Labbe C, Zaidi H, Morel C (updated by Thielemans K, Imanet H Ltd), *STIR Description of the STIR implementation of FBP 3DRP* Version 0.91: http://stir.sourceforge.net/documentation/STIR-FBP3DRP.pdf (2004) pp.1-10.

50. Comanor K, Virador P, Moses W. Algorithms to Identify Detector Compton Scatter in PET Modules. *IEEE Trans Nucl Sci* 1996; NS-43: 2213-8.

51. Kinahan P, Rogers J. Analytic 3D image reconstruction using all detected events. *IEEE Trans Nucl Sci* 1989; 36: 964-8.

52. Zaidi H, Hasegawa B. Determination of the Attenuation Map in Emission Tomography. *J Nucl Med* 2003; 44: 291-315.

53. Bailey D, Jones T, Spinks T. A method for measuring the absolute sensitivity of positron emission tomographic scanners. *Eur J Nucl Med* 1991; 18: 374-9.

54. Hubbel J, Seltzer S. *Tables of X-ray mass attenuation coefficients and mass energy absorption coefficients 1keV to 20MeV for elements Z=1 to 92 and 48 additional substances of dosimetric interest.* U.S. Department of Commerce. NISTIR 5632 (1995).

55. Hoffman EJ, Cutler PD, Digby WM and Mazziotta JC. 3-D phantom to simulate cerebral blood flow and metabolic images for PET. *IEEE Trans Nucl Sci* 1990; 37: 616-20.

56. *OpenGATE Collaboration*, Users Guide V6.1: Voxelized Source and Phantom: http://www.opengatecollaboration.org.

57. Grammaticos P, Fountos G. The physician should benefit, not harm the patient. *Hell J Nucl Med* 2006; 9(2): 82-4.

58. Barone R, Borson-Chazot F, Valkema R et al. Patient-specific dosimetry in predicting renal toxicity with ^{90}Y-DOTATOC: relevance of kidney volume and dose rate in finding a dose-effect relationship. *J Nucl Med* 2005; 46: 99S-106S.

59. Kwekkeboom DJ, Krenning EP, Lebtahi R et al. The Mallorca Consensus Conference participants. ENETS Consensus Guidelines for the Standards of Care in Neuroendocrine Tumors: Peptide Receptor Radionuclide Therapy with Radiolabeled Somatostatin Analogs. *Neuroendocrinol* 2009; 90: 220-6.

60. Otte A, Jermann E, Behe M et al. DOTATOC: A powerful new tool for receptor mediated radionuclide therapy. *Eur J Nucl Med* 1997; 24: 792-6.

61. Safford SD, Coleman RE, Gockerman JP et al. Iodine-131 meta-iodobenzylguanidine treatment for metastatic carcinoid. Results in 98 patients. *Cancer* 2004; 101: 1987-93.

62. Shapiro B, Sisson JC, Wieland DM et al. Radiopharmaceutical therapy of malignant pheochromocytoma with I-131 MIBG: results from 10 years of experience. *J Nucl Biol Med* 1991; 35: 269-76.

63. Shreve PD, Anzai Y, Wahl RL. Pitfalls in oncologic diagnosis with FDG-PET imaging: physiologic and benign variants. *RadioGraphics* 1999; 19: 61-77.

64. Bombardieri E, Aktolun C, Baum RP et al. [67]*Ga scintigraphy procedure guidelines for tumour imaging*. European Association of Nuclear Medicine (EANM) Guidelines 2003, pp.1-9.

65. Krenning EP, Bakker WH, Kooij PP et al. Somatostatin receptor scintigraphy with indium-111-DTPA-D-Phe-1-octreotide in man: metabolism, dosimetry and comparison with iodine-123-Tyr-3-octreotide. *J Nucl Med* 1992; 33: 652-8.